SPOT5-HRS digital elevation models and the monitoring of glacier elevation changes in North-West Canada and South-East Alaska

Etienne Berthier [a,*], Thierry Toutin [b,1]

[a] *CNRS-LEGOS, 14 av E. Belin, 31400 Toulouse, France*
[b] *Canada Center for Remote Sensing/Natural Resources Canada 588 Booth Street Ottawa Ontario, Canada K1A 0Y7*

Abstract

Monitoring the response of land ice to climate change requires accurate and repeatable topographic surveys. The SPOT5-HRS (High Resolution Stereoscopic) instrument covers up to 120 km by 600 km in a single pass and has the potential to accurately map the poorly known topography of most glaciers and ice caps. The acquisition of a large HRS archive over ice-covered regions is planned by the French Space Agency (CNES) and Spotimage, France during the 2007–2008 International Polar Year (IPY). Here, we report on the accuracy and value of HRS digital elevation model (DEM) over ice and snow surfaces.

A DEM is generated by combining tools available from CNES with the PCI Orthoengine[SE] software, using HRS images acquired in May 2004 over South-East Alaska (USA) and northern British Columbia (Canada). The DEM is evaluated through comparison with shuttle radar topographic mission (SRTM) DEM and ICESAT data, on and around the glaciers. A horizontal shift of 50 m is found between the HRS and SRTM DEMs and is attributed to errors in the SRTM DEM. Over ice-free areas, HRS elevations are 7 m higher than those of SRTM, with a standard deviation of ±25 m for the difference between the two DEMs. The 7-m difference is partly attributed to the differential penetration of the electromagnetic waves (visible for HRS; microwave for SRTM) in snow and vegetation.

We also report on the application of sequential DEMs (SRTM DEM in February 2000 and HRS DEM in May 2004) for the monitoring of glacier elevation changes. We map the topographic changes induced by a surge of one tributary of Ferris Glacier. Maximum surface lowering of 42 (±10) m and rising of 77 (±10) m are observed in the 4 years time interval. Thinning rates up to 10 (±2.5) m/yr are observed at low altitudes and confirm the ongoing wastage of glaciers in South-East Alaska.

© 2007 Elsevier Inc. All rights reserved.

Keywords: Glacier; Ice cap; Climate change; Glacier surge; International Polar Year; Topography; DEM; SPOT5; SRTM; ICESAT; Alaska; British Columbia

1. Introduction

Mass loss of mountain glaciers, ice caps and ice sheets are estimated to account for one third of the current 3 mm/yr of sea level rise (Cazenave, 2006; Kaser et al., 2006). Repeated topographic surveys of these ice masses are needed to better constrain (or update) this estimate and to monitor the dynamic evolution of the cryosphere in response to climate change.

Accurate glacial topography is required for glaciology and remote-sensing research. A digital elevation model (DEM) is essential for image processing steps such as (Kääb et al., 2005): (i) orthorectification of images to obtain maps and derive surface velocity fields; (ii) correction of the influence of topography on image radiometry and; (iii) delimitation of glacier drainage basins and debris-covered glaciers. DEMs (and the corresponding hypsographic curves) are also needed for glaciological field studies to convert sparse measurements of ablation and accumulation to the annual specific mass balance of the whole glacier (Paterson, 1994).

Synthetic aperture radar images acquired with slightly different viewing angles can be processed interferometrically to retrieve a DEM (Li and Goldstein, 1990; Toutin and Gray, 2000).

* Corresponding author. Tel.: +33 5 61 33 29 66.
  E-mail addresses: etienne.berthier@legos.obs-mip.fr (E. Berthier),
thierry.toutin@ccrs.nrcan.gc.ca (T. Toutin).
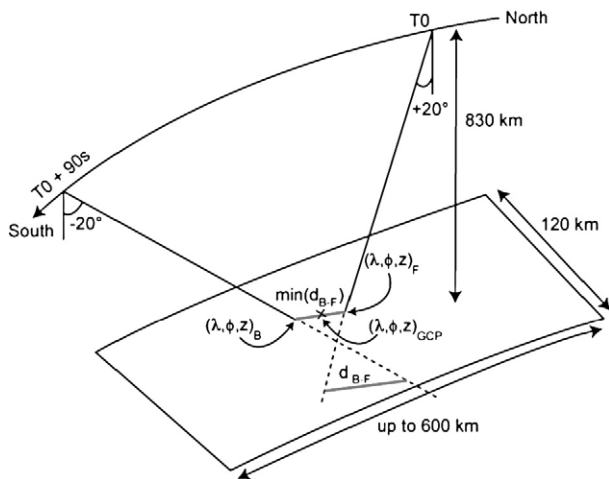 [1] Tel.: +1 613 947 1293.

Fig. 1. HRS acquisition geometry (adapted from Bouillon et al., 2006). Images with a swath of 120 km along a segment up to 600 km are acquired during a descending (North ➔ South) orbit. This figure also illustrates how the ground coordinates of a ground control point $(\lambda, \phi, z)_{GCP}$ are found by minimizing the distance (d_{B-F}) between the two lines of sight $(\lambda, \phi, z)_F$ and $(\lambda, \phi, z)_B$ originating from the fore- and back-looking image coordinates of one tie point.

This technique was used during the shuttle radar topographic mission (SRTM) to map most continental surfaces between 56°S and 60°N (Rabus et al., 2003). However, the SRTM dataset does not cover the polar regions (North of 60°N and South of 56°S) where most ice masses are located. Additional elevation data over large regions would likewise be useful to fill holes in SRTM data and survey polar regions.

Glacier DEMs can also be derived from space-borne optical sensors: SPOT1-4 and SPOT5-HRG (high resolution geometric) acquire pairs of cross-track (from two different orbits) stereoscopic images, typically separated by several days (Berthier et al., 2004). The time separation severely limits the use of these sensors for large scale mapping because of radiometric variations between the multi-date images (Toutin, 2004; Toutin and Cheng, 2002) and frequent cloud cover over mountainous and polar regions. Furthermore, glacier flow (up to a few meters per day) during this interval can bias the topographic measurement. Consequently, large scale mapping of ice-covered regions is easier using optical sensors acquiring real-time (along-track) stereoscopic pairs such as Terra-ASTER, SPOT5-HRS or ALOS-PRISM. Since 2000, ASTER has been acquiring 15-m resolution stereoscopic images and DEMs have been derived with a grid spacing of 30 m and a vertical accuracy of 15–25 m (Toutin, 2002; Welch et al., 1998). Numerous applications of ASTER DEMs over mountain glaciers have been reported within the Global Land Ice Measurement from Space (GLIMS) project (Kääb, 2005; Kargel et al., 2005; Toutin, in press) and also over the fast-flowing glaciers of the Antarctic and Greenland ice sheets (Howat et al., 2007; Stearns and Hamilton, 2007).

HRS, on board SPOT5, also acquires along-track stereoscopic images (Fig. 1). HRS only provides panchromatic images but has several advantages over ASTER and other SPOT data:

(1) The image swath is 120 km, two times wider than other SPOT or ASTER images. Regions up to 120×600 km² (72,000 km²) can be observed in a single pass of the satellite. A large swath area is crucial when monitoring ice caps and icefields covering as much as 90,000 km² in South-East Alaska (Arendt et al., 2002) or 150,000 km² in the Canadian archipelago (Dyurgerov and Meier, 2005).

(2) HRS has a high resolution (10 m). However, the image pixel size is smaller along track (5 m) than across track (10 m) to increase the accuracy of the DEMs (Bouillon et al., 2006).

(3) The two stereoscopic images are acquired with a ±20° fore- and aft-viewing angles which lead to a base-to-height (B/H) ratio of 0.8 compared to 0.6 for ASTER. This higher sensitivity to the topography increases the DEM accuracy but could also lead to larger mismatched areas in steep regions where strong stereoscopic distortions of the images may limit their correlation.

Since the launch of SPOT5 in 2002, mainly ice-free regions have been observed by HRS and large scale DEMs have been produced by the French Mapping Agency (IGN, Institut Géographique National). The acquisition of HRS stereo-pairs over ice-covered regions (mostly polar ice caps and the margins of the two major ice sheets) is planned by the French Space Agency (CNES, Centre National d'Etudes Spatiales) and Spotimage, France during the International Polar Year (IPY) in 2007–2009 (except for regions south of 81°S and north of 81°N that are not visible from SPOT5 orbit).

On ice-free terrain, for a single pair of HRS images, the horizontal accuracy has been 15 m at the 68% confidence level (LE68) and the vertical accuracy better than 5 m in medium relief areas, and around 10 m in areas of higher relief (Bouillon et al., 2006; Toutin, 2006). To assess the accuracy and value of this sensor for glaciological research, we evaluated HRS data acquired in May 2004 for large icefields located in North-West British Columbia (Canada) and South-East Alaska (Molnia, 2007). This image pair was provided as a courtesy by Spotimage and chosen because it was acquired with the low gain needed to avoid sensor saturation (Table 1). One of the two HRS images (covering 120×200 km²) is displayed in Fig. 2.

The outline of our study is as follows. First we describe the processing chain for an HRS image pair and the generation of a DEM using SPOT5 acquisition parameters (position and attitude of the satellite/sensor) only. We then evaluate the relative accuracy of this DEM over ice-free regions by comparing it to an SRTM DEM and ICESat laser altimetric data. Finally, we report on some of our observed glacier elevation changes detected with the SRTM and HRS DEMs.

Table 1
Characteristics of the HRS images used in this study

Acquisition date	10 May 2004
Ground sampling distance	5 m along-track/10 m cross-track
Swath/length	120 km/200 km
Panchromatic band	0.48–0.70 μm
Fore/aft-viewing angle	+/−20°
Gain	1

2. Generation of HRS DEM

Software available from CNES and the Orthoengine^{SE} module of PCI Geomatica are combined to compute the HRS DEM in two steps. First, the CNES software is used to determine automatically the ground coordinates of about 50 tie points (TPs) spread all over the stereo-images. Then, this set of ground control points (GCPs) is imported into Orthoengine^{SE} to compute the HRS stereo model and the DEM. A similar methodology has been used to derive a DEM from SPOT5-HRG images over Himalaya (Berthier et al., 2007). The improvement over this previous study is that here no existing cartographic data and DEM are required to generate GCPs. Consequently, the method can be readily applied to all regions on Earth.

GCPs are distinctive terrain features with known ground coordinates and good visibility on the images (so defined by their column and line positions). They are used to compute or refine the stereo model, and, consequently, are needed to produce a DEM. Traditionally, GCP ground coordinates are derived from maps or field surveys (*e.g.* using Differential Global Positioning System, DGPS). Because accurate maps are lacking for most ice-covered regions and field surveys are not always feasible, the GCPs derived here are based on the knowledge of SPOT5 acquisition parameters (position and attitude of the satellite/sensor) and the stereoscopic intersection of the two lines of sight (Spotimage, 2002). The following paragraphs explain how these GCPs are generated by, first, collecting TPs on the images and, second, by finding their ground coordinates.

Fifty (50) TPs distributed over the stereo-pair were identified as topographic features such as summits, nunataks, river beds, and road intersections that were clearly defined on both images, and span a large range of altitudes. The line of sight for each image of the stereo-pair was computed for each TP using the acquisition parameters provided in the HRS metadata (Spotimage, 2002) (Fig. 1). If the image acquisition parameters were exactly known and each TP represented precisely the same feature in both images, the HRS fore- and back-looking lines of sight should intersect in one point on the ground. Due to the uncertainties in the acquisition parameters of the two images and the difficulty to pick exactly the same feature in the two images of the stereo-pair (referred to here as "image pointing"), the lines of sight do not intersect in a point. Consequently, to find the (unique) ground coordinates of each TP (noted $[\lambda, \phi, z]_{TP}$ with λ the longitude, ϕ the latitude and z the altitude), all possible elevations (0 to 5000 m in our region) were scanned to determine the altitude (z_{TP}) that minimized the horizontal distance d_{B-F} between the fore- and back-looking lines of sight (Fig. 1):

$$d_{B-F} = \sqrt{(\lambda_B - \lambda_F)^2 + (\varphi_B - \varphi_F)^2}$$

where $(\lambda, \phi)_F$ and $(\lambda, \phi)_B$ are the ground coordinates for the fore-looking and the back-looking images, respectively.

The ground coordinates $(\lambda, \phi)_{TP}$ of each TP were then calculated as the average of the fore- and back-looking coordinates (along the line of sight) at the altitude z_{TP}:

$$\lambda_{TP} = \frac{(\lambda_B(z_{TP}) + \lambda_F(z_{TP}))}{2}$$

$$\varphi_{TP} = \frac{(\varphi_B(z_{TP}) + \varphi_F(z_{TP}))}{2}$$

At this stage, each TP is characterized by its image (column and line) and ground (λ, ϕ, z) coordinates and thus corresponds to a GCP to be input in Orthoengine^{SE} for the second step.

GCP accuracy is limited by the errors in image pointing (ability to pick exactly the same feature in the two images) and the uncertainties of the SPOT5 acquisition parameters. For our 50 GCPs, the minimum of d_{B-F} ranged from 0.1 to 11.5 m with a mean value of 5.6 m and a standard deviation of 2.4 m. These values are in the range of the image pointing errors (0.5 to 1 image pixel) indicating that limited error originates from the acquisition parameters. This is expected as the two images were acquired along the same orbit. Introducing numerous GCPs
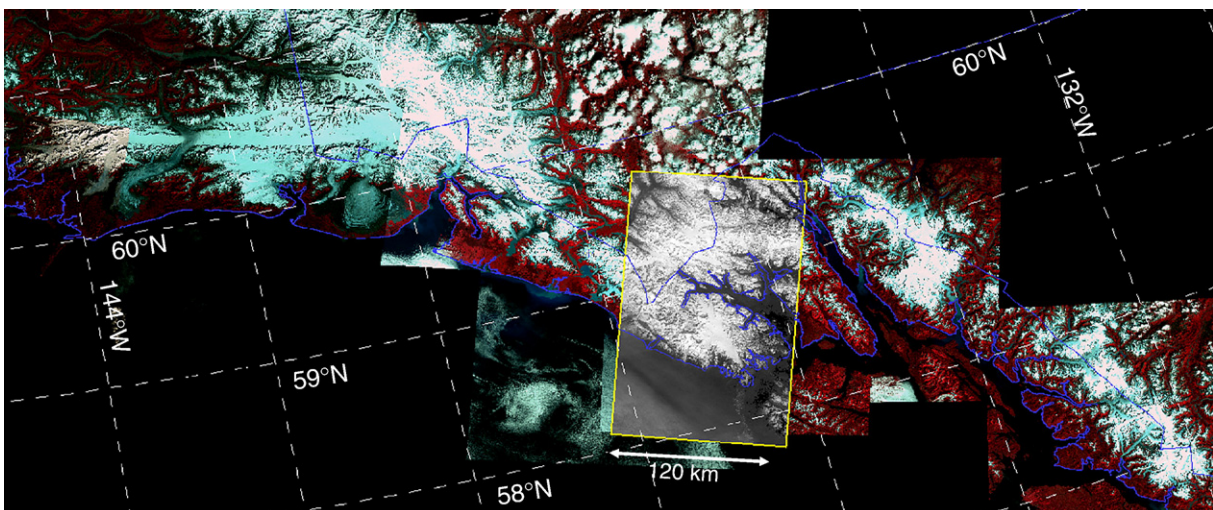

Fig. 2. Study area: the Glacier Bay region (59°N, 137°W). One of the two HRS images acquired in May 2004 is embedded here in a Landsat 2000–2001 mosaic of South-East Alaska, North-West British Columbia (BC) and South-West Yukon Territory (YT). The coastline and the boarder between Alaska, BC and YT are overlaid in blue. (© CNES 2006; distribution Spotimage). (For interpretation of the references to colour in this figure legend, the reader is referred to the web version of this article.)
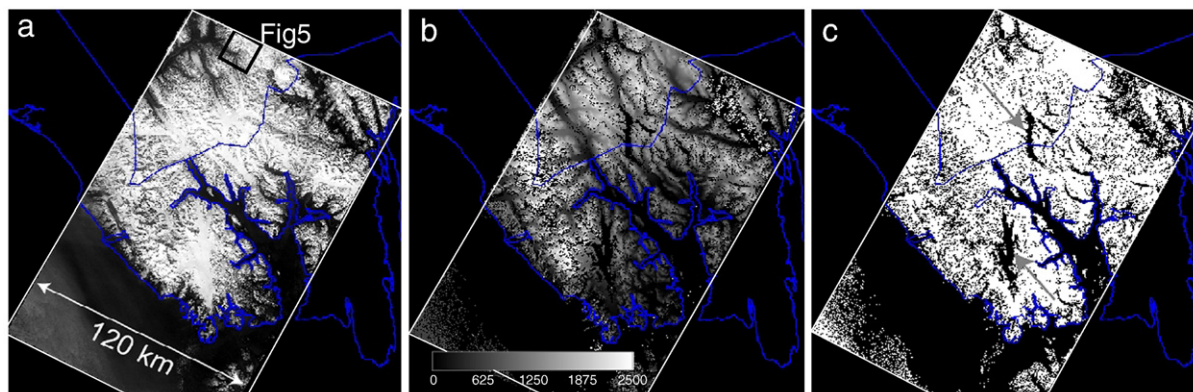
Fig. 3. (a) The HRS backward looking image. Note the important snow cover on most of the scene. The black rectangle locates the area shown in Fig. 5; (b) The HRS-derived DEM. The mismatched areas are displayed in black. Altitudes range from sea level to over 4000 m; (c) Mask associated with the DEM. In white, regions where the DEM was computed; in black, regions where the correlation failed leading to mismatched areas in the DEM. The grey arrows locate two large icefields (Brady in the South, Carroll in the North) where the lack of radiometric contrast led to large mismatched areas in the DEM. (© CNES 2006; distribution Spotimage).

(here 50) reduced the propagation of image pointing (random) errors in the computation of the final stereo model using a least-squares adjustment process (Toutin, 2006). Our set of GCPs is characterized by a good internal consistency, however absolute horizontal errors (LE68) of 15 m (due to errors in the satellite position and attitude) are expected for SPOT5-HRS (Bouillon et al., 2006).

The GCPs were imported into PCI Orthoengine^{SE} to compute the SPOT5 stereo model (Toutin, 2001, 2006). The 3D physical sensor modeling was originally developed to suit the geometry of push-broom scanners, such as SPOT1 (Toutin, 1983), and has been subsequently adapted at the Canada Centre for Remote Sensing (CCRS) as an integrated and unified geometric modeling to geometrically process multi-sensor stereo/block data (Toutin, 2004, 2006). Based on good quality GCPs, the accuracy of this model is within one-third of a pixel for medium-resolution images, better than one pixel for high-resolution (HR) images and one resolution cell for radar images, as long as there is no extrapolation in planimetry and altimetry.

The two quasi-epipolar images generated from the raw images with the previously-computed stereo-model were then cross-correlated at each pixel using multi-scale mean normalized cross-correlation method, with sub-pixel computation of the maximum of the correlation coefficient to compute the elevation parallaxes. Pixels were flagged as mismatched when their correlation score (which ranges from 0 to 100) was lower than 50. The terrain elevations were finally derived from the elevation parallaxes using the previously-computed stereo-model. At this stage, two different DEMs were generated. The first one, HRS#1, was computed by keeping mismatched areas during the cross-correlation and even by increasing the size of these gaps (*Eroding* function of Orthoengine^{SE}). The justification for the latter operation is that DEM elevations close to the mismatched areas are less reliable. HRS#1 is useful for elevation change mapping, as it contains only calculated values of elevations and no interpolation of sometimes large mismatched areas. For the second DEM, HRS#2, interpolation was used to fill the mismatched areas in regions where the correlation failed. Both DEMs were then filtered using a 3×3 median filter (to remove outliers) and a 3×3

boxcar filter to smooth the topography and avoid step-like artifacts observed in PCI-Geomatica DEMs (S. Guðmundsson, personal communication). The DEMs were projected in the B.C. province Albers Conical Equal Area map projection with a 50-m ground spacing[2] (BC Ministry of Environment, 1992).

The HRS#1 DEM is presented in Fig. 3 with a mask (right panel) over the mismatched areas (30% of the land surface). Once water bodies were excluded (nearly 8000 km^2 or 34% of the image), the mismatched areas covered 30% of the land surface (4550 km^2 out of 15,350 km^2). Small mismatched areas on the HRS#1 DEM were observed on steep slopes where the stereoscopic distortions between the fore- and aft-view were too strong. Other mismatched areas were due to the presence of thin clouds that changed position and shape in the 90 s time interval separating the two acquisitions. The largest mismatched areas were observed in the accumulation zones of the Brady Icefield and Carroll Glacier (Fig. 3). Saturation of the optical device is not the cause because the lowest available gain was used during these HRS acquisitions. Rather, they correspond to areas that lacked radiometric contrast, thus impeding image correlation. The lack of contrast is due to the significant amount of snow covering the glaciers in May, at the beginning of the ablation season (Ramage and Isacks, 2003).

Data gaps similar to those found on Brady Icefield and Carroll Glacier would severely limit the value of HRS acquisitions during IPY. However, we believe that this effect will be reduced by planning HRS acquisitions close to the end of the ablation season when the snow cover is densest and dust-covered, and has reached its maximum degree of surface texture. For example, a high quality DEM was derived from SPOT5-HRG images acquired in late August 2003 in the accumulation area of the Mer de Glace in the French Alps (Berthier et al., 2004). A lower sun illumination angle will also improve the correlation over flat snow-covered regions because it increases the texture of the images by enhancing the sensitivity of the reflectivity to micro-topography (Lodwick and Paine, 1985; Toutin, 2001). A nearly complete topographic coverage of the

---

[2] Defined at http://srmwww.gov.bc.ca/gis/bceprojection.html.

western Vatnajökull ice cap (Iceland) has been obtained previously from SPOT5-HRG images acquired two days apart in early October 2004 when the sun elevation was only 19° (Berthier et al., 2006b). Comparatively, the sun elevation was 49° for the HRS data used in the present study.

3. Accuracy of the HRS DEM over ice-free regions

3.1. Horizontal accuracy

A previous study using HRS images for ice-free terrain reported an absolute horizontal accuracy (LE68) of 15 m (Bouillon et al., 2006). Because the same sensor model was used to derive our set of GCPs, we expect a similar accuracy. We compared the HRS DEM to the SRTM DEM to test this expectation as 90% of SRTM DEM tiles in North America are reported to have an absolute horizontal accuracy of 12.6 m (Rodriguez et al., 2006). The location performance of HRS was also tested using independent planimetric data coverage of roads.

The SRTM DEM of our study area was obtained by merging 12 tiles, each covering 1° by 1° (SRTM3, version 2, downloaded at *ftp://e0srp01u.ecs.nasa.gov*). The original grid spacing of SRTM3 is 3″, corresponding to about 92 m in latitude and 52 m in longitude for our study area. We reprojected the SRTM DEM to the same 50-m Albers Conical Equal Area map projection.

The mean horizontal shift between the HRS DEM and the SRTM DEM was calculated as the shift that minimizes the standard deviation of the difference between the two DEMs on ice-free regions (Berthier et al., 2007; Rodriguez et al., 2006). We noted a shift of one pixel (50 m) in the Easting direction and 0.2 pixel (10 m) in the Northing direction between both DEMs (Fig. 4). We then attempted to determine which DEM contains the major source of positional error.

One advantage afforded by the HRS data (compared to SRTM) is that the ortho-images can be used to identify visible features such as road networks, buildings, or other objects. Both
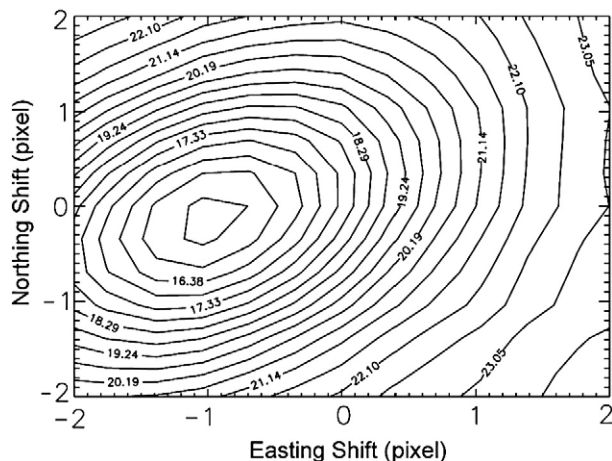

Fig. 4. Contour plot of the standard deviation (in meters) of the elevation difference {HRS-SRTM} on ice-free regions for different shifts in easting and northing. The coordinates of the minimum in the contour plot indicate the mean horizontal shift between the two DEMs.

HRS raw images were orthorectified at a 10-m posting using the HRS#2 DEM. As the two HRS stereo images were acquired with nonvertical and opposite incidence angles (±20°), a vertical error in the HRS DEM (δz) will approximately lead to a horizontal shift of tan $(\pm 20°)*\delta z = \pm 0.36*\delta z$. This error has an opposite sign for the two ortho-images and, therefore, the horizontal shift between the two ortho-images can be used to detect regions where DEM elevations are wrong. Consequently, the horizontal accuracy of the HRS sensor model (and DEM) can be assessed using the HRS ortho-images on: (i) regions where both HRS ortho-images present a limited horizontal shift (indicating small elevation errors in the HRS DEM); and (ii) where human-built features such as roads or buildings, whose ground coordinates are known, can be clearly identified on the images. Due to the remoteness of our study area, only one large road, was visible on the northern part of our HRS stereo-pair, and has been surveyed by the Canadian government[3] with circular map accuracy (90%) better than 10 m.

The road vector data were overlaid on both HRS ortho-images (Fig. 5). Where the road turns to a nearly East–West direction at the northern edge (upper part in Fig. 5), a systematic shift in the South–North direction of 1–2 pixels (10 to 20 m) was observed. Because the same systematic shift was present in both HRS ortho-images, this shift was attributed to geopositioning error of the HRS sensor model. In addition, the North–South oriented line-road was well-located on both ortho-images, indicating very small errors (less than 10 m) in the East–West direction. These observations imply that most of the East–West offset observed between the HRS DEM and the SRTM DEM was due to errors in the latter data set, at least in the northern part of the images.

For further comparison, the HRS DEM was kept unchanged and the SRTM DEM was resampled (using a bicubic filter) to correct the calculated shift (50 m in the Easting direction and 10 m in the Northing direction). A good registration of the two DEMs is crucial before analyzing surface elevation differences: in steep regions, even a small horizontal shift (here one pixel or 50 m) can lead to large, erroneous elevation differences (Fig. 6).

3.2. Vertical accuracy

The two co-registered DEMs have been subtracted to analyze the elevation differences on the ice-free regions. Glacier outlines are needed to distinguish between ice-covered and ice-free regions. Existing outlines derived from USGS and BC government maps have been used (Larsen et al., 2007) and, where large changes occurred, updated to 2000–2001 using Landsat images.[4] Note that our HRS images of May 2004 were not suitable for glacier outline mapping due to snow cover.

We summarized some of the major differences between the HRS (#1 and #2) and SRTM DEMs in Table 2. To compute these statistics, we excluded pixels whose absolute elevations differed by more than 100 m. These anomalous HRS elevations

---

[3] Vector "shapefile" downloaded at http://www.geobase.ca.
[4] Landsat images available from the Geographic Information Network of Alaska at http://www.gina.alaska.edu.
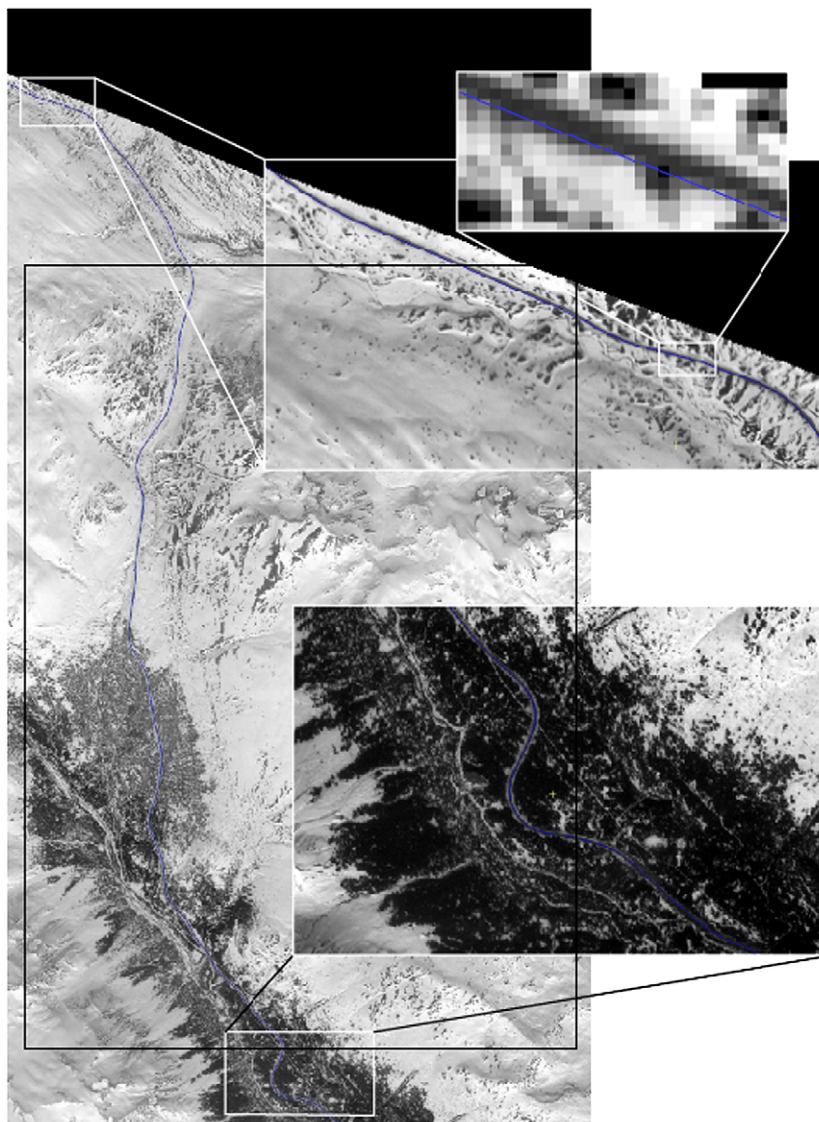
Fig. 5. Location of a road in British Columbia (in blue) over the northern part of the orthorectified aft-viewing HRS image. The ground pixel sampling of the image is 10 m. The detailed views on the right panels highlight the good co-registration of the two datasets and a shift of 1 to 2 pixels (10 to 20 m) in the northernmost part of the HRS images. (© CNES 2006; distribution Spotimage). (For interpretation of the references to colour in this figure legend, the reader is referred to the web version of this article.)

were mainly due to clouds. The standard deviation was smaller for HRS#1 (25 m) than for HRS#2 (28 m) due to the interpolation of mismatched areas in HRS#2. These results are worse than previously obtained by Bouillon et al. (2006) (around 10 m in high relief) but our study site was more challenging (*e.g.* steeper). Also, we compared our HRS DEM with a reference DEM (SRTM) that is less accurate in high mountain regions (Berthier et al., 2006a). As in the case of ASTER DEMs (Toutin, 2002) and SRTM DEMs (Surazakov and Aizen, 2006), the standard deviation of the differences between HRS#1 and SRTM was positively correlated with slope (not shown), which is consistent with previous studies (Toutin, 2006).

The mean differences indicate that both HRS DEMs (HRS#1 and HRS#2) are higher than SRTM by about 7 to 9 m on ice-free regions. We suspect that a portion of the observed differences in mean elevation is explained by the presence of snow on the ground

at the time of acquisition of the HRS images. Snow cover is clearly visible on the images and is confirmed by the climate record at the Haines Nw weather station[5] (250 m a.s.l.) where the mean average snow depth in April is close to 0.8 m. Moreover, at the Moore Creek Bridge station[6] (59°35′N, 135°12′W, 570 m a.s.l., 50 km from Haines Nw, so slightly outside of our study area) 2.1 m of snow was recorded on 24 April 2004 and 1.7 m remained on 31 May 2004. Furthermore, the precipitation pattern over the Glacier Bay regions shows a strong dependence with elevation.[7] So, deeper snow is predicted at higher elevations than at Haines Nw or Moore Creek Bridge. This is confirmed by glaciological field measurements where winter accumulation is reported to reach

---

[5] 59°27'N, 136°21'W, http://www.wrcc.dri.edu/cgi-bin/cliMAIN.pl?ak3504.
[6] http://www.wcc.nrcs.usda.gov/cgibin/snow_rpt.pl?state=alaska.
[7] See map at http://www.wrcc.dri.edu/pcpn/ak.gif.
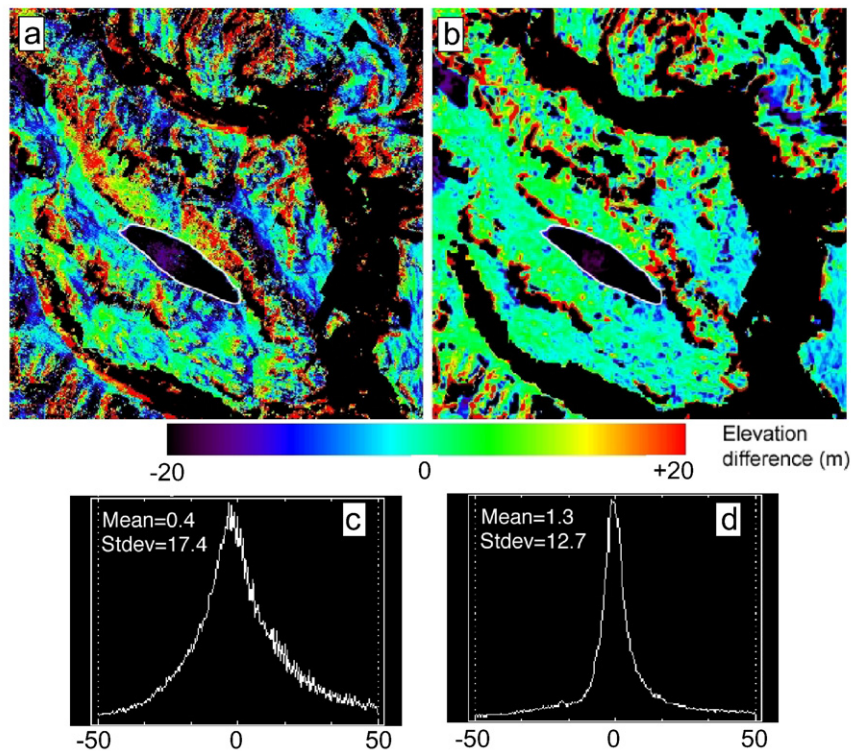
Fig. 6. Maps and histograms of the elevation differences {HRS#1−SRTM} over a 20∗20 km^2 sub-region. The left panels (a and c) show the elevation differences prior to any horizontal shift. The right panels (b and d) show the elevation differences after co-registrating SRTM to the HRS DEM. A small glacier (Burroughs) in the central part of the image (surrounded by a white contour) has been excluded from the histograms. Absolute elevation differences larger than 50 m have been excluded. The figure illustrates the reduction (by nearly 30%) in the standard deviation of elevation differences once a good co-registration of the DEM is reached.

4 m/yr water equivalent (w.e.) which corresponds to 10 m of snow if a density of 400 kg/m^3 is assumed (Eisen et al., 2001; Motyka et al., 2003; Pelto and Miller, 1990).

It is likely that snow cover was also present during the acquisition of SRTM data in February 2000. However, the C-band (5.6 cm wavelength) radar signal, which was used during the mission, is known to penetrate through unmetamorphosed snow (Papa et al., 2002; Rignot et al., 2001) while HRS panchromatic band does not penetrate. Consequently, penetration of the radar signal in the cold snow layer of February 2000 is expected to limit the elevation bias (top of snow vs. bare earth) in the SRTM DEM for ice-free terrain.

On the other hand, previous studies have shown that SRTM interferometric elevations do not represent the summit of vegetation but rather the mean scattering phase center height located between the ground surface and the top of the vegetation (Kellndorfer et al., 2004). This is due to the interaction of the relatively short C-band wavelength with various scatterers associated with leaves, branches and ground. For example, in the forests of California and Georgia (USA) penetration reaches

5–10 m (Kellndorfer et al., 2004). In our case, similar penetration would lead to underestimated SRTM elevations compared to HRS elevations, which are based on the top-of-the-canopy reflectance, and could thus contribute to the systematic differences between the DEMs over ice-free regions. The C-band penetration depends on the density of scatterers (Toutin and Amaral, 2000). To our knowledge, this effect has never been studied and quantified for the boreal forests of South-East Alaska or British Columbia where the canopy height can reach 30–50 m (Larsen et al., 2007).

The spatial pattern of elevation differences between the HRS and SRTM DEMs is now analyzed for more specific areas (Fig. 7). The SRTM DEM is higher than the HRS DEM except on low elevation glacier tongues (see Section 4.1) and an ice-free sub-region (labeled A in Fig. 7) where HRS#1 is systematically lower by ca. 5–10 m. To assess the origin of the bias on sub-region A, we compared both DEMs to ICESat (Ice, Cloud, and Land Elevation Satellite) elevation profiles (Zwally et al., 2002). ICESat data have already been used regionally (Surazakov and Aizen, 2006) and globally (Carabajal and Harding, 2005) to assess the accuracy of the SRTM DEM. Over South-East Alaska and North-West B.C., there were few ICESat data, presumably due to persistent cloud cover (Sauber et al., 2005). We compared all 604 footprints which were available for the small sub-region A (20 by 20 km^2) between September 2003 (laser period 2A) and March 2006 (laser period 3E) (Fig. 8). ICESat data were referenced to the Topex/Poseidon datum which differs slightly from the WGS-84 datum used for SRTM

Table 2

Statistics on the elevation differences between the two HRS DEMs (HRS#1 with mismatched areas eroded and HRS#2 with all mismatched areas filled by interpolation) and the SRTM DEM on the ice-free regions

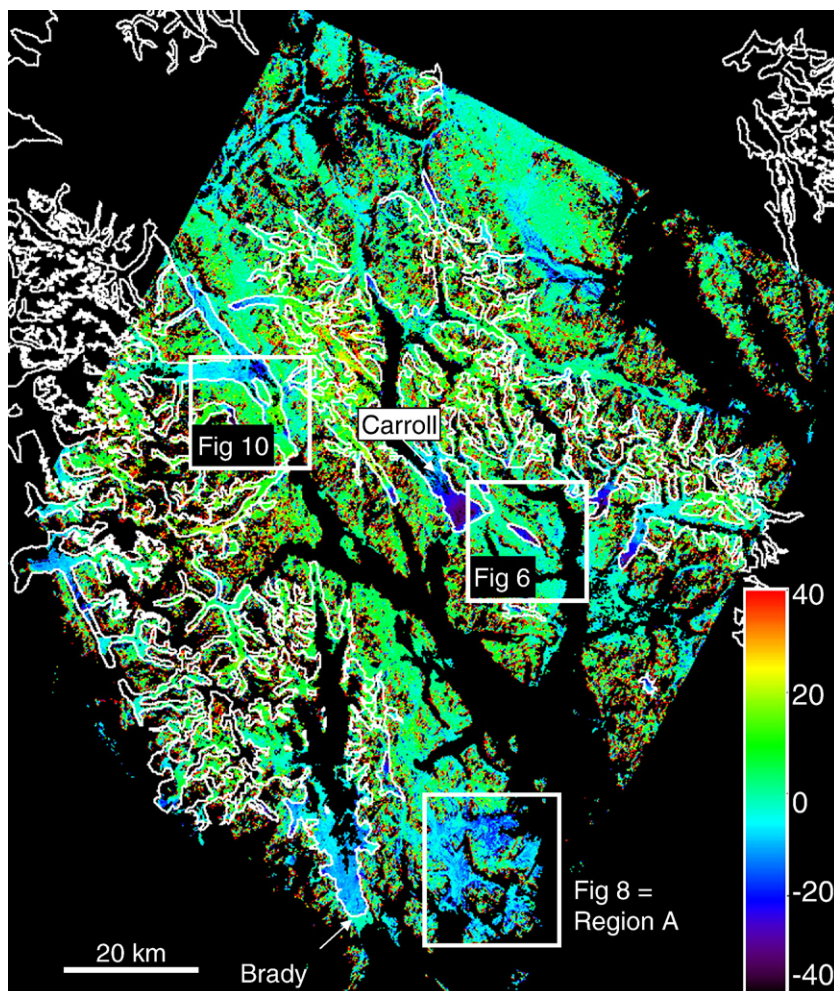|	Mean difference (m)	Standard deviation (m)	Sample size
HRS#1−SRTM	7.1	25	2,338,186
HRS#2−SRTM	9.5	28	2,755,001

Fig. 7. Map of the elevation differences (in meters) between February 2000 (SRTM DEM) and May 2004 (HRS DEM) over the whole region surveyed by HRS in May 2004. Glacier outlines have been overlaid in white.

and HRS. The horizontal datum conversion and the transformation from ellipsoidal height to altitude above the EGM96 geoid were performed using software distributed by the National Snow and Ice Data Center.[8] For each laser footprint (covering about 70 m), the corresponding DEM elevation was extracted by bilinear interpolation. All data points for which the elevation differences (with SRTM or HRS) were greater than 100 m were considered as blunders and removed (Carabajal and Harding, 2005). After this exclusion, 201 points remained. HRS#1 is only 3 m higher than ICESat whereas SRTM is nearly 9 m higher (Table 3). The standard deviations are comparable for the two DEMs (~10 m). For sub-region A, we can conclude that the local bias between HRS and SRTM is mainly due to errors in SRTM.

4. Glacier elevation changes using SRTM and HRS data

Glacier surface elevation changes during four years (between February 2000 and May 2004) were measured by differencing the SRTM and HRS DEMs. Given the relative random and systematic errors between the two DEMs (Table 2), only absolute elevation changes larger than 10 m were statistically significant (Etzelmüller, 2000).

4.1. Elevation changes with altitude

The map of elevation differences between 2000 and 2004 is shown in Fig. 7. The elevation changes on ice-covered regions are also displayed as a function of altitude after averaging by altitude interval of 100 m (Fig. 9).

At low elevations (below 500 m a.s.l.), glaciers thinned on average by almost 10 m. Brady, Carroll and Burroughs glaciers, thinned by up to 40 (±10) m at their front over the 4.25 year period (Figs. 6 and 7). The long-term rate (1948–1999 for Alaska; 1985–1999 for British Columbia) of glacier downwasting reported for this region (Larsen et al., 2007; Schiefer et al., 2007) continued in the first four years of the twenty first century.

A systematic thickening of the glaciers is observed above 500 m a.s.l. (Fig. 9). The apparent thickening can be attributed both to the snow cover during HRS acquisition and the
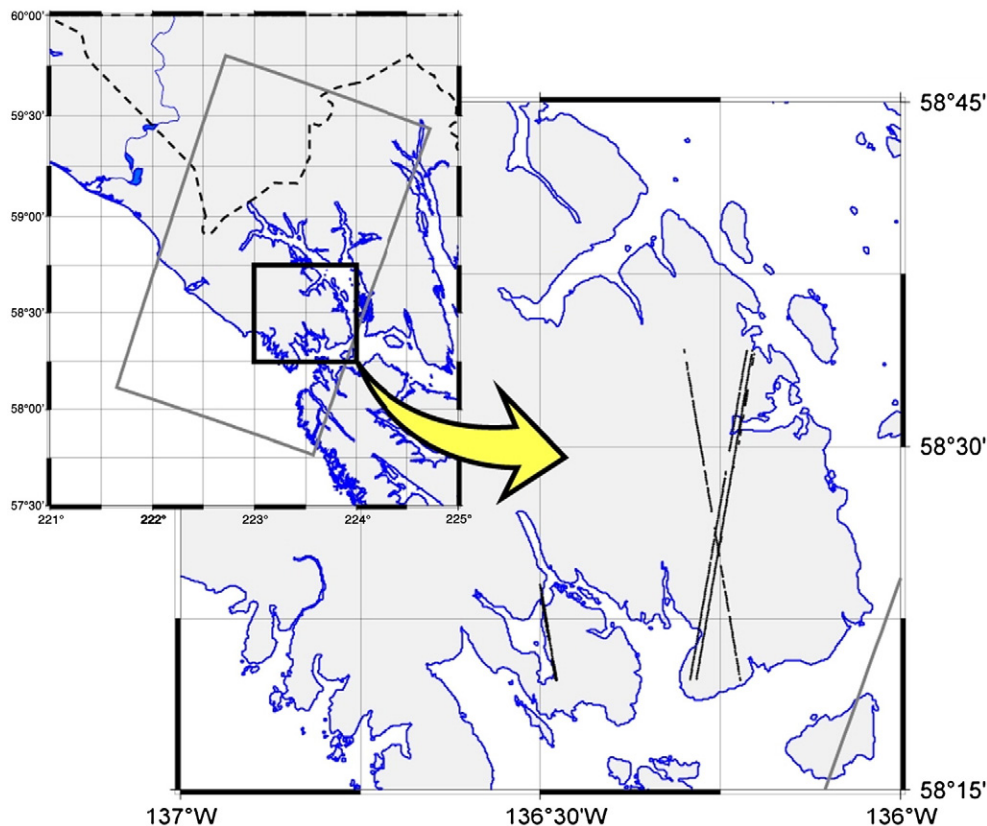
Fig. 8. Location of the ICESat tracks available for sub-region A (located in Fig. 7). The laser period plotted here are 2A, (release 26), 2B, 3A, 3B, 3D, and 3E (release 28) available from September 2003 to February 2006. Overall, 600 laser footprints are available for this sub-region, but only 200 remained once the cloud detection algorithm has been applied.

penetration of the SRTM C-band radar signal through the cold snow of February 2000. The difference is higher (nearly 20 ± 10 m) on glaciers than on ice-free regions (7 to 9 ± 10 m) probably because of the altitudinal gradient of the precipitation (Section 3.2) combined with the fact that glaciers are mainly located at higher elevations.

To study the volumetric change of glaciers, sequential DEMs should be acquired near the end of the ablation season (Paterson, 1994). Our data were from the middle (SRTM) and at the end (HRS) of the winter. Consequently, we do not report on a total glacier volume change that would mainly reflect seasonal variations.

4.2. Elevation changes experienced by surging glaciers

Many glaciers of South-East Alaska, Yukon Territory and Northern British Columbia are described as surge-type (Clarke

and Holdsworth, 2002a, b). The life cycle of a surging glacier is characterized by an active phase with a rapid transfer of mass from the upper "reservoir" area to the lower "receiving" area, and ice velocities that increase by a factor of 10 to 100. During the quiescent phase, ice flow rates decline substantially and the reservoir area builds up again (Paterson, 1994). Together with field studies (Björnsson, 1998), new remote-sensing observations could help better understand the timing of this phenomenon (Magnusson et al., 2005).

Here, the elevation changes induced by a surge were clearly depicted for a tributary of Ferris Glacier (South of Grand Pacific Glacier in the Fairweather Mountains). Over the four-year period, the glacier thinned by up to 42 m along its central portion when its snout thickened by 77 m where it coalesces with Ferris Glacier (Fig. 10). A complex pattern of crevasses and the formation of a bulge near its terminus are clear signs that the surge is fully developed in May 2004. The absence of these patterns on an August 2000 Landsat image indicates that the surge started later than summer 2000.

We estimated the volume of ice that was transferred during the surge by defining the area of the reservoir (and receiving region) to include all regions which experienced thinning (or thickening). They covered 5.6 km^2 and 2.7 km^2, respectively. Multiplying the reservoir and receiving areas by their mean elevation changes (-18 ± 10 m and $+36 \pm 10$ m respectively) led to the redistributed ice volume. The two numbers agree within

Table 3
Statistics on the elevation differences between the two large-scale DEMs (SRTM or HRS#1) and ICESat profiles available for the small ice-free sub-region A (located in Figs. 7 and 8) where a systematic difference has been observed between HRS#1 and SRTM

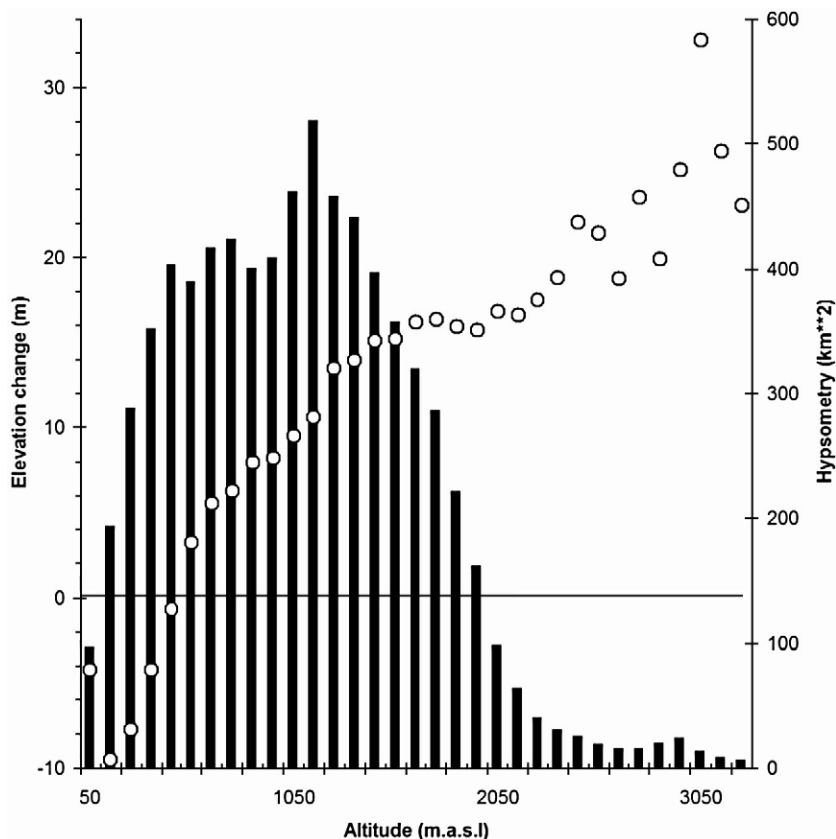|	Mean difference (m)	Standard deviation (m)	Sample size
SRTM–ICESat	8.7	10.5	201
HRS#1–ICESat	3.0	11.4	201

Fig. 9. Elevation changes (m) as a function of altitude for the ice-covered regions (circle). Each point corresponds to the mean elevation change within an altitude interval of 100 m. For each altitude range, a Gaussian filtering has been applied to removed outliers (Berthier et al., 2004). The standard deviation of the elevation differences is about 20 m. The black histograms show the hypsometry of these ice-covered regions (in km^2).

5% and indicate that 0.1 ($\pm$0.005) km^3 of ice was transferred during the surge.

5. Discussion and conclusions

HRS images have the potential for accurate and repeatable topographic surveys of ice-covered regions. DEMs can be generated without the need to collect GCPs from maps or in the field and, consequently, HRS data are most valuable for remote regions. Our HRS DEM of South-East Alaska had a vertical accuracy of $\pm$25 m (LE68), which is not as good as previous HRS DEMs obtained over medium topography (Bouillon et al., 2006; Toutin, 2006). This is because we dealt with an ice-covered region in a challenging mountainous topography with no accurate cartographic data. Additional work is now needed to assess the accuracy of HRS DEMs over the relatively gentle slopes close to
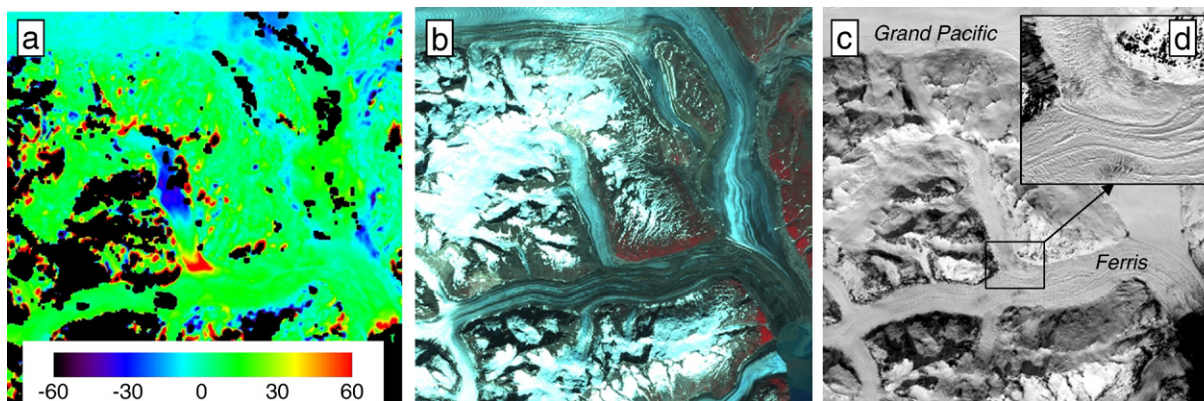

Fig. 10. Surge of a tributary of Ferris Glacier. (a) Elevation changes (m) induced by the surge. Note that the upper basin of the glacier was not affected by the surge; (b) Landsat image acquired 10 August 2000; (c) HRS image of May 2004. A highly crevassed glacier surface, the formation of a bulge at the front and the deformation of the central moraine of Ferris Glacier (see details in panel d) are clear confirmation that the glacier has surged. (© CNES 2006; distribution Spotimage).

the margins of the polar ice sheets. Together with the DEM, 10 m resolution HRS ortho-images with an absolute horizontal accuracy of ±10–20 m have been generated.

For ice-free regions, the HRS DEM is ~7–9 m higher than the SRTM DEM. This difference is partly attributed to the presence of snow on the ground in May 2004 when the HRS images were acquired. Partial penetration of the SRTM C-band radar signal through the canopy is another potential explanation to this difference. This mean difference is not constant throughout the DEMs. For example, HRS is lower than SRTM by 5 to 10 m for a 20 km by 20 km ice-free sub-region. For this sub-region, HRS-derived elevations are in good agreement with accurate ICESat altimetric data. The combination of large scale HRS DEMs with accurate but sparse ICESat profiles is a promising avenue for future research. This research, however, will require an extensive analysis of the spatial pattern of elevation changes for stable regions surrounding ice masses in addition to any elevation changes of glaciers and ice sheets.

If cloud-free images are available, the main limitation of HRS data in glaciology is the difficulty in retrieving elevations for flat portion of the largest icefields due to the lack of radiometric contrast. Better results may be obtained in the future by scheduling satellite acquisitions at the end of the ablation season (September in the Northern hemisphere) when the snow transformation is important and the sun is lower above the horizon.

We studied changes in the elevation of glacier surfaces by differencing the May 2004 HRS DEM and the February 2000 SRTM DEM. In particular a tributary of Ferris glacier surged over this time period, and transferred 0.1 km^3 of ice between its central portion and its terminus. At their lowest elevations, most glaciers thinned at rates (about 10 m/yr) comparable to longer-term estimates reported by previous authors (Larsen et al., 2007; Schiefer et al., 2007). Higher HRS than SRTM derived elevations above 500 m a.s.l. may be caused by differential signal penetrations through the snow, and therefore probably reflect a seasonal artifact, due to the deep (over 10 m) winter snow layer.

A large archive of HRS images is being acquired by CNES and Spotimage during the International Polar Year (2007 and 2008) and large scale DEMs will be derived for ice-covered regions. Their time separation with the SRTM DEM (7 to 8 years) or early ASTER stereo data (launched in 2000) will probably permit a reassessment of net glacier volume changes over this time period at the regional scale, at least for glacier/icefield masses known to experience rapid changes in elevation such as the Patagonia Icefields and South-East Alaska. This large archive may also result in a benchmark topography of many ice masses for comparison with future satellite topographic missions such as Cryosat2 or Tandem-X.

Acknowledgements

References

Arendt, A. A., Echelmeyer, K. A., Harrison, W. D., Lingle, C. S., & Valentine, V. B. (2002). Rapid wastage of Alaska glaciers and their contribution to rising sea level. *Science, 297*(5580), 382−386.

Berthier, E., Arnaud, Y., Baratoux, D., Vincent, C., & Remy, F. (2004). Recent rapid thinning of the "Mer de Glace" glacier derived from satellite optical images. *Geophysical Research Letters, 31*(L17401). doi:10.1029/2004GL020706

Berthier, E., Arnaud, Y., Kumar, R., Ahmad, S., Wagnon, P., & Chevallier, P. (2007). Remote sensing estimates of glacier mass balances in the Himachal Pradesh (Western Himalaya, India). *Remote Sensing of Environment, 108*(3), 327−338.

Berthier, E., Arnaud, Y., Vincent, C., & Remy, F. (2006a). Biases of SRTM in high-mountain areas: Implications for the monitoring of glacier volume changes. *Geophysical Research Letters, 33*(L08502). doi:10.1029/2006GL025862

Berthier, E., Bjornsson, H., Palsson, F., Feigl, K. L., Llubes, M., & Remy, F. (2006b). The level of the Grimsvötn subglacial lake, Vatnajökull, Iceland, monitored with SPOT5 images. *Earth and Planetary Science Letters, 243*(1−2), 293−302.

Björnsson, H. (1998). Hydrological characteristics of the drainage system beneath a surging glacier. *Nature, 395*(6704), 771−774.

Bouillon, A., Bernard, M., Gigord, P., Orsoni, A., Rudowski, V., & Baudoin, A. (2006). SPOT 5 HRS geometric performances: Using block adjustment as a key issue to improve quality of DEM generation. *ISPRS Journal of Photogrammetry and Remote Sensing, 60*(3), 134−146.

British Columbia Ministry of Environment, Land and Parks. (1992). *British Columbia specifications and guidelines for geomatics, release 2.0.* Victoria, B. C., Canada.

Carabajal, C. C., & Harding, D. J. (2005). ICESat validation of SRTM C-band digital elevation models. *Geophysical Research Letters, 32*(L22S01). doi:10.1029/2005GL023957

Cazenave, A. (2006). How fast are the ice sheets melting? *Science, 314*(5803), 1250−1252.

Clarke, G. K. C., & Holdsworth, G. (2002a). Glaciers of the Coast Mountains. In R. S. William & J. G. Ferrigno (Eds.), *Satellite image atlas of glaciers of the world* (pp. J301−J311). North America: U.S. Geological Survey Professional Paper.

Clarke, G. K. C., & Holdsworth, G. (2002b). Glaciers of the St. Elias Mountains. In R. S. William & J. G. Ferrigno (Eds.), *Satellite image atlas of glaciers of the world* (pp. J301−J311). North America: U.S. Geological Survey Professional Paper.

Dyurgerov, M. B., & Meier, M. F. (2005). *Glaciers and the changing earth system: A 2004 snapshot.* Boulder: INSTAAR Occasional Paper #58 Available at: http://instaar.colorado.edu/other/download/OP58dyurgerov-meier.pdf

Eisen, O., Harrison, W. D., & Raymond, C. F. (2001). The surges of Variegated Glacier, Alaska, USA, and their connection to climate and mass balance. *Journal of Glaciology, 47*(158), 351−358.

Etzelmüller, B. (2000). On the quantification of surface changes using grid-based digital elevation models (DEMs). *Transactions in Geographical Information Systems, 4*(2), 129−143.

Howat, I. M., Joughin, I., & Scambos, T. A. (2007). Rapid changes in ice discharge from Greenland outlet glaciers. *Science*, *315*(5818), 1559−1561. doi:10.1126/science.1138478

Kääb, A. (2005). Combination of SRTM3 and repeat ASTER data for deriving alpine glacier flow velocities in the Bhutan Himalaya. *Remote Sensing of Environment*, *94*(4), 463−474.

Kääb, A., Huggel, C., Fischer, L., Guex, S., Paul, F., Roer, I., et al. (2005). Remote sensing of glacier- and permafrost-related hazards in high mountains: An overview. *Natural Hazards and Earth System Sciences*, *5*(4), 527−554.

Kargel, J. S., Abrams, M. J., Bishop, M. P., Bush, A., Hamilton, G., Jiskoot, H., et al. (2005). Multispectral imaging contributions to global land ice measurements from space. *Remote Sensing of Environment*, *99*(1−2), 187−219.

Kaser, G., Cogley, J. G., Dyurgerov, M. B., Meier, M. F., & Ohmura, A. (2006). Mass balance of glaciers and ice caps: Consensus estimates for 1961–2004. *Geophysical Research Letters*, *33*(L19501). doi:10.1029/2006GL027511

Kellndorfer, J., Walker, W., Pierce, L., Dobson, C., Fites, J. A., Hunsaker, C., et al. (2004). Vegetation height estimation from shuttle radar topography mission and national elevation datasets. *Remote Sensing of Environment*, *93*(3), 339−358.

Larsen, C. F., Motyka, R. J., Arendt, A. A., Echelmeyer, K. A., & Geissler, P. E. (2007). Glacier changes in southeast Alaska and northwest British Columbia and contribution to sea level rise. *Journal of Geophysical Research*, *112*(F01007). doi:10.1029/2006JF000586

Li, C. K., & Goldstein, R. M. (1990). Studies of multibaseline spaceborne interferometric synthetic aperture radars. *IEEE Transactions on Geoscience and Remote Sensing*, *28*(1), 88−97.

Lodwick, G. H., & Paine, S. H. (1985). A digital elevation model of the Barnes ice-cap derived from Landsat-MSS data. *Photogrammetric Engineering and Remote Sensing*, *51*(12), 1937−1944.

Magnusson, E., Bjornsson, H., Dall, J., & Palsson, F. (2005). Volume changes of Vatnajokull ice cap, Iceland, due to surface mass balance, ice flow, and subglacial melting at geothermal areas. *Geophysical Research Letters*, *32*(L05504). doi:10.1029/2004GL021615

Molnia, B. F. (2007). Late nineteenth to early twenty-first century behavior of Alaskan glaciers as indicators of changing regional climate. *Global and Planetary Change*, *56*(1−2), 23−56.

Motyka, R. J., O'Neel, S., Connor, C. L., & Echelmeyer, K. A. (2003). Twentieth century thinning of Mendenhall Glacier, Alaska, and its relationship to climate, lake calving, and glacier run-off. *Global and Planetary Change*, *35*(1−2), 93−112.

Papa, F., Legresy, B., Mognard, N. M., Josberger, E. G., & Remy, F. (2002). Estimating terrestrial snow depth with the Topex-Poseidon altimeter and radiometer. *IEEE Transactions on Geoscience and Remote Sensing*, *40*(10), 2162−2169.

Paterson, W. S. B. (1994). *The physics of glaciers (3rd ed.)*. New York: Pergamon.

Pelto, M. S., & Miller, M. M. (1990). Mass balance of the Taku Glacier, Alaska, from 1946 to 1986. *Northwest Science*, *64*, 121−130.

Rabus, B., Eineder, M., Roth, A., & Bamler, R. (2003). The shuttle radar topography mission — A new class of digital elevation models acquired by spaceborne radar. *ISPRS Journal of Photogrammetry and Remote Sensing*, *57*(4), 241−262.

Ramage, J. M., & Isacks, B. L. (2003). Interannual variations of snowmelt and refreeze timing on southeast-Alaskan icefields, U.S.A. *Journal of Glaciology*, *49*(164), 102−116.

Rignot, E., Echelmeyer, K., & Krabill, W. (2001). Penetration depth of interferometric synthetic-aperture radar signals in snow and ice. *Geophysical Research Letters*, *28*(18), 3501−3504. doi:10.1029/2000GL012484

Rodriguez, E., Morris, C. S., & Belz, J. E. (2006). A global assessment of the SRTM performance. *Photogrammetric Engineering and Remote Sensing*, *72*(3), 249−260.

Sauber, J., Molnia, B., Carabajal, C., Luthcke, S., & Muskett, R. (2005). Ice elevations and surface change on the Malaspina Glacier, Alaska. *Geophysical Research Letters*, *32*(L23S01). doi:10.1029/2005GL023943

Schiefer, E., Menounos, B., & Wheate, R. (2007). Recent volume loss of British Columbian glaciers, Canada. *Geophysical Research Letters*, *34*(L16503). doi:10.1029/2007GL030780

Spotimage (2002). *SPOT Satellite geometry handbook*.

Stearns, L. A., & Hamilton, G. S. (2007). Rapid volume loss from two East Greenland outlet glaciers quantified using repeat stereo satellite imagery. *Geophysical Research Letters*, *34*(L05503). doi:10.1029/2006GL028982

Surazakov, A. B., & Aizen, V. B. (2006). Estimating volume change of mountain glaciers using SRTM and map-based topographic data. *IEEE Transactions on Geoscience and Remote Sensing*, *44*(10), 2991−2995.

Toutin, Th. (1983). Analyse mathématique des capacités stéréoscopiques du satellite SPOT. *Diplôme d'Etudes Approfondies* (pp. 74). Paris, France: Ecole Nationale des Sciences Géodésiques.

Toutin, Th. (2001). Elevation modelling from satellite visible and infrared (VIR) data. *International Journal of Remote Sensing*, *22*(6), 1097−1125.

Toutin, Th. (2002). Three-dimensional topographic mapping with ASTER stereo data in rugged topography. *IEEE Transactions on Geoscience and Remote Sensing*, *40*(10), 2241−2247.

Toutin, Th. (2004). Comparison of stereo-extracted DTM from different high-resolution sensors: SPOT-5, EROS-A, IKONOS-II, and QuickBird. *IEEE Transactions on Geoscience and Remote Sensing*, *42*(10), 2121−2129.

Toutin, Th. (2006). Generation of DSMs from SPOT-5 in-track HRS and across-track HRG stereo data using spatiotriangulation and autocalibration. *ISPRS Journal of Photogrammetry and Remote Sensing*, *60*(3), 170−181.

Toutin, Th. (in press). ASTER DEMs for geomatic and geoscientific applications: A review. *International Journal of Remote Sensing*.

Toutin, Th., & Amaral, S. (2000). Stereo RADARSAT data for canopy height in Brazilian forest. *Canadian Journal of Remote Sensing*, *26*(3), 189−199.

Toutin, Th., & Cheng, P. (2002). Comparison of automated digital elevation model extraction results using along-track ASTER and across-track SPOT stereo images. *Optical Engineering*, *41*(9), 2102−2106.

Toutin, Th., & Gray, L. (2000). State-of-the-art of elevation extraction from satellite SAR data. *ISPRS Journal of Photogrammetry and Remote Sensing*, *55*(1), 13−33.

Welch, R., Jordan, T., Lang, H., & Murakami, H. (1998). ASTER as a source for topographic data in the late 1990's. *IEEE Transactions on Geoscience and Remote Sensing*, *36*(4), 1282−1289.

Zwally, H. J., Schutz, B., Abdalati, W., Abshire, J., Bentley, C., Brenner, A., et al. (2002). ICESat's laser measurements of polar ice, atmosphere, ocean, and land. *Journal of Geodynamics*, *34*(3−4), 405−445.